Gauging low-dose X-ray phase-contrast imaging at a single and large propagation distance

Ralf Hofmann, Alexander Schober, Steffen Hahn, Julian Moosmann, Jubin Kashef, Madeleine Hertel, Venera Weinhardt, Daniel Haenschke, Lukas Helfen, Ivan A. Sanchez Salazar, et al.

Gauging low-dose X-ray phase-contrast imaging at a single and large propagation distance

Ralf Hofmann,[1,*] Alexander Schober,[1] Steffen Hahn,[1] Julian Moosmann,[1] Jubin Kashef,[1] Madeleine Hertel,[1] Venera Weinhardt,[2] Daniel Hänschke,[1] Lukas Helfen,[3] Iván A. Sánchez Salazar,[1] Jean-Pierre Guigay,[3] Xianghui Xiao,[4] and Tilo Baumbach[1,5]

[1]*Institute for Photon Science and Synchrotron Radiation, Karlsruhe Institute of Technology, Hermann-von-Helmholtz-Platz 1, D-76344 Eggenstein-Leopoldshafen, Germany*
[2]*Centre for Organismal Studies (COS), Universität Heidelberg, Im Neuenheimer Feld 230, 69120 Heidelberg, Germany*
[3]*European Synchrotron Radiation Facility, 6 rue Jules Horowitz, 38000 Grenoble, France*
[4]*Advanced Photon Source, Argonne National Laboratory, 9700 South Cass Avenue, Argonne, IL 60439, USA*
[5]*Laboratory for Applications of Synchrotron Radiation, Karlsruhe Institute of Technology, Postfach 6980, D-76128 Karlsruhe, Germany*
[*]*ralf.hofmann2@kit.edu*

Abstract: The interactions of a beam of hard and spatio-temporally coherent X-rays with a soft-matter sample primarily induce a transverse distribution of exit phase variations $\delta\phi$ (retardations or advancements in pieces of the wave front exiting the object compared to the incoming wave front) whose free-space propagation over a distance z gives rise to intensity contrast g_z. For single-distance image detection and $|\delta\phi| \ll 1$ all-order-in-z phase-intensity contrast transfer is linear in $\delta\phi$. Here we show that ideal coherence implies a decay of the (shot-)noise-to-signal ratio in g_z and of the associated phase noise as $z^{-1/2}$ and z^{-1}, respectively. Limits on X-ray dose thus favor large values of z. We discuss how a phase-scaling symmetry, exact in the limit $\delta\phi \to 0$ and dynamically unbroken up to $|\delta\phi| \sim 1$, suggests a filtering of g_z in Fourier space, preserving non-iterative quasi-linear phase retrieval for phase variations up to order unity if induced by multi-scale objects inducing phase variations $\delta\phi$ of a broad spatial frequency spectrum. Such an approach continues to be applicable under an assumed phase-attenuation duality. Using synchrotron radiation, *ex* and *in vivo* microtomography on frog embryos exemplifies improved resolution compared to a conventional single-distance phase-retrieval algorithm.

OCIS codes: (340.7440) X-ray imaging; (350.5030) Phase; (270.5290) Photon statistics.

References and links

1. J. Moosmann, A. Ershov, V. Altapova, T. Baumbach, M. S. Prasad, C. LaBonne, X. Xiao, J. Kashef, and R. Hofmann, "X-ray phase-contrast in vivo microtomography probes novel aspects of *Xenopus* gastrulation," Nature **497**, 374–377 (2013).
2. J. Moosmann, A. Ershov, V. Weinhardt, T. Baumbach, M. S. Prasad, C. LaBonne, X. Xiao, J. Kashef, and R. Hofmann, "Time-lapse X-ray phase-contrast microtomography for in vivo imaging and analysis of morphogenesis," Nat. Protoc. **9**, 294–304 (2014).

#251990 Received 16 Oct 2015; revised 25 Jan 2016; accepted 28 Jan 2016; published 19 Feb 2016

3. B. L. Henke, E. M. Gullikson, and J. C. Davis, "X-ray interactions: photoabsorption, scattering, transmission, and reflection at E=50-30000 eV, Z=1-92," At. Data. Nucl. Data Tables **54**, 181–342 (1993).
4. N. Rohani, L. Canty, O. Luu, F. Fagotto, and R. Winklbauer, "EphrinB/EphB Signalling Controls Embryonic Germ layer Separation by Contact-Induced Cell Detachment," PLoS Biol. **9**, e1000597 (2011).
5. S. F. S. Becker, R. Mayor, and J. Kashef, "Cadherin-11 Mediates Contact Inhibition of Locomotion during *Xenopus* Neural Crest Cell Migration," PLoS ONE **8**(12), e85717 (2013).
6. M. Mickoleit, B. Schmid, M. Weber, F. O. Fahrbach, S. Hombach, S. Reischauer, and J. Huisken, "High-resolution reconstruction of the beating zebrafish heart, " Nat. Methods **11**, 919–922 (2014).
7. J. C. Maxwell, *A Treatise on Electricity and Magnetism* (Oxford Clarendon Press, 1873).
8. C. Huygens, T. Young, and A.-J. Fresnel, *The Wave Theory of Light: Memoirs of Huygens, Young, and Fresnel* (American Book Company, 1900).
9. A. Snigirev, I. Snigireva, I., V. Kohn, S. Kuznetsov, and I. Schelokov, "On the possibilities of X-ray phase contrast microimaging by coherent high-energy synchrotron radiation," Rev. Sci. Instrum. **66**, 5486–5493 (1995).
10. S. W. Wilkins, T. E. Gureyev, D. Gao, A. Pogany, and A. W. Stevenson, "Phase-contrast imaging using polychromatic hard X-rays," Nature **384**, 335–338 (1996).
11. K. A. Nugent, T. E. Gureyev, D. F. Cookson, D. M. Paganin, and Z. Barnea,"Quantitative phase imaging using hard X rays," Phys. Rev. Lett. **77**, 2961–2964 (1996).
12. A. Momose, T. Takeda, Y. Itai, and K. Hirano, "Phase-contrast X-ray computed tomography for observing biological soft tissues," Nat. Medicine **2**, 473–475 (1996).
13. C. David, B. Nöhammer, H. H. Solak, and E. Ziegler, "Differential phase-contrast imaging using a shearing interferometer," Appl. Phys. Lett. **81**, 3287–3289 (2002).
14. T. Weitkamp, A. Diaz, C. David, F. Pfeiffer, M. Stampanoni, P. Cloetens, and E. Ziegler, "X-ray phase imaging with a grating interferometer," Opt. Express **13**, 6296–6304 (2005).
15. F. Pfeiffer, T. Weitkamp, O. Bunk, and C. David, "Phase retrieval and differential phase-contrast imaging with low-brilliance X-ray sources," Nat. Phys. **2**, 258–261 (2006).
16. P. Cloetens, *Contribution to Phase Contrast Imaging, Reconstruction and Tomography with Hard Synchrotron Radiation: Principles, Implementation and Applications* (PHD thesis Vrije Universiteit Brussel, 1999).
17. L. Waller, L. Tian, and G. Barbastathis, "Transport of intensity phase-amplitude imaging with higher order intensity derivatives," Opt. Express **18**, 12552–12561 (2010).
18. J.-P. Guigay, "Fourier transform analysis of Fresnel diffraction patterns and in-line holograms," Optik **49**, 121–125 (1977).
19. J. Moosmann, R. Hofmann, and T. Baumbach, "Nonlinear phase retrieval from single-distance radiograph," Opt. Express **18**, 25771–25785 (2010).
20. J. Moosmann, R. Hofmann, and T. Baumbach, "Single-distance phase retrieval at large phase shifts," Opt. Express **19**, 12066–12073 (2011).
21. R. Hofmann, J. Moosmann, and T. Baumbach, "Criticality in single-distance phase retrieval," Opt. Express **19**, 25881–25890 (2011).
22. L. D. Landau, "The theory of the Fermi liquid," Sov. J. Phys. JETP **3**, 920 (1957).
23. R. Hofmann, *The Thermodynamics of Quantum Yang-Mills Theory: Theory and Applications* (World Scientific Publishing Co., 2012).
24. S. Hahn, R. Hofmann, and T. Baumbach are preparing a manuscript to be called "Analysis of Fresnel diffraction: the Gaussian phase."
25. D. M. Paganin, *Coherent X-Ray Optics* (Oxford University, 2006).
26. S. Hahn, R. Hofmann, J. Moosmann, O. Öktem, L. Helfen, J.-P. Guigay, Th. van de Kamp, and T. Baumbach, "Contrast transfer in propagation based X-ray phase-contrast imaging," (to be published in Phys. Rev. A).
27. M. Born and E. Wolf, *Principles of Optics*, 7th edition (Cambridge University, 1999).
28. E. Wolf, *Introduction to the Theory of Coherence and Polarization of Light* (Cambridge University, 2007).
29. A. Ruhlandt, M. Krenkel, M. Bartels, and T. Salditt, "Three-dimensional phase retrieval in propagation-based phase-contrast imaging," Phys. Rev. A **89**, 033847 (2014).
30. B. Sixou, "Regularization Methods for Phase Retrieval and Phase Contrast Tomography, Abstr. Appl. Anal. **2015**, 943501 (2015).
31. X. Wu, H. Liu, and A. Yan, "X-ray phase-attenuation duality and phase retrieval," Opt. Lett. **30**, 379–381 (2005).
32. D. M. Paganin, S. C. Mayo, T. E. Gureyev, P. R. Miller, and S. W. Wilkins, "Simultaneous phase and amplitude extraction from a single defocused image of a homogeneous object," J. Microsc. **206**, 33–40 (2002).
33. M. Langer, P. Cloetens, A. Pacureanu, and F. Peyrin, "X-ray in-line phase tomography of multimaterial objects," Opt. Lett. **37**, 2151–2153 (2012).
34. M. Langer, P. Cloetens, B. Hesse, H. Suhonen, A. Pacureanu, and F. Peyrin, "Priors for X-ray in-line phase contrast tomography of heterogeneous objects," Phil. Trans. R. Soc. A **372**, 20130129 (2014).
35. R. C. Chen, H. L. Xie, L. Rogon, R. Longo, E. Castelli, and T. Q. Xiao, "Phase retrieval in quantitative x-ray microtomography with a single sample-to-detector distance," Opt. Lett. **36**, 1719–1721 (2011).
36. P. Kirkpatrick and A. V. Baez, "Formation of Optical Images by X-Rays," J. Opt. Soc. Amer. **38**, 766–774 (1948).

#251990 Received 16 Oct 2015; revised 25 Jan 2016; accepted 28 Jan 2016; published 19 Feb 2016

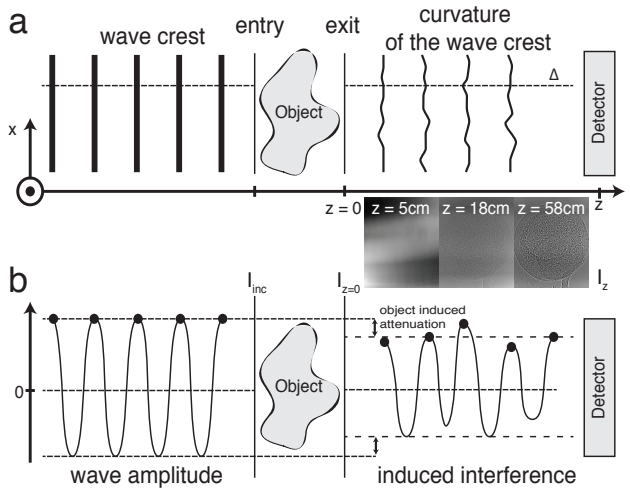

Fig. 1. Principle of image formation in propagation based phase-contrast X-ray radiography. (a) snapshot of a 2D slice through a set-up where a perfect plane wave of constant intensity I_{inc} impinges on an object. Locally curved and attenuated wave fronts exit the object at $z = 0$ with intensity $I_{z=0}$. Even without object attenuation self-interference induces inhomogeneous intensity I_z in the detector plane at $z > 0$ (propagated projections at varying z of a fixed stage-12 *Xenopus laevis* embryo, see Appendix B). (b) representation of wave amplitude along dashed line Δ in (a). Object induced attenuation is indicated by a drop of amplitude at $z = 0$.

1. Introduction

Due to their penetrating power, hard X-rays allow for genuine three-dimensional structural and functional imaging of entire organisms. In particular, vertebrate model embryos such as *Xenopus laevis* (optically opaque) can be imaged *in vivo* in four dimensions and with micrometer spatial resolution, appealing to X-ray phase contrast [1, 2]. As early developmental stages are composed of light elements only, essentially, such embryos act as pure-phase objects from an imaging point of view ($\delta/\beta \sim 10^3$ [3] for X-ray energies $E \sim 30\,\mathrm{GeV}$, δ, β representing the projected refractive index $n = 1 - \delta + \mathrm{i}\beta$ ($\delta = \delta(\mathbf{x})$, $\beta(\mathbf{x}) > 0$, real). Note, however, that non-vanishing values of β can pose a severe dose problem, in particular for tomography where many projections of the object are required. Presently, established light microscopy methods are applied in developmental biology to investigate embryonic cell and tissue dynamics both using explanted wildtype tissue *in vitro* [4] and genetically manipulated (functional modification [5] and fluorescent proteins [6]) entire specimen. Note that fluorescence microscopy, albeit chemically sensitive, does not provide dense structural information and is limited to peripheral cell layers even for optically translucent specimen.

The theory of propagation based X-ray phase-contrast imaging assumes beamlike electromagnetic waves [7] described by Fresnel theory [8], paraxiality simplifying the field content and dynamics of Maxwell's equations: a complex, scalar wave field ψ_z satisfies a Schrödinger equation in two transverse spatial dimensions ($\mathbf{x}_\perp$, coordinates orthogonal to optical axis) and one temporal (z, coordinate along optical axis) dimension. The thus presumed dominance of transverse variations of ψ_z over longitudinal ones plays out, e.g., when transmitted wavefronts in hard and coherent X-rays free-space propagate [9–11], see Fig. 1.

Because of their large oscillation frequencies, quantitative assessments of the advancement/retardation of pieces in the exit X-ray wave front ($z = 0$) (relative phase variations $\delta\phi$)

#251990 Received 16 Oct 2015; revised 25 Jan 2016; accepted 28 Jan 2016; published 19 Feb 2016

must be retrieved from temporally averaged interference effects as manifested by intensity variations in a transverse plane $z > 0$. To determine the exit phase map ϕ from a full-field intensity measurement, various possibilities exist, e.g., the use of grating interferometry [12–15] or a multi-distance defocussing method [16, 17]. For *in vivo* tomography, repeated exposures under one and the same projection angle are, however, dose prohibitive and often not commensurate with rates of cell motion in the living specimen. Phase retrieval from a single-distance full-field intensity measurement with a sufficiently low noise-to-signal ratio (NSR), as induced by free-space propagation of the exit wave field for large values of z, then is the only feasible route. To interpret such intensity data quantitatively, a thorough understanding of contrast transfer between exit phase and intensity throughout a potentially non-linear regime of phase variations is required. Optimal tomographic reconstruction of the object aims at (i) a maximum of spatial resolution at a minimum of dose, (ii) best possible sensitivity to phase variations, and (iii) a computationally efficient algorithm to enable large and well monitored throughput. In the following we denote the incident intensity and intensity detected at propagation distance z by I_{inc} and I_z, respectively (Fig. 1). Given a (static) sample and an X-ray detection system, the attainment of an optimal intensity contrast $g_z = (I_z - I_{\mathrm{inc}})/I_{\mathrm{inc}}$ depends on beam coherence (spatial and temporal), photon flux density (temporal resolution), z, and dose (NSR). The present paper intents to tackle this optimization problem by investigating the z dependence of the NSR in g_z and ϕ when the smallness of phase variations $\delta\phi$ cannot be assumed.

Even under ideal conditions an exact inversion of the contrast transfer from ϕ to g_z is impossible [18]: a local expansion of this relation invokes non-linearities, including infinitely high powers of transverse derivatives [19]. Therefore, large phase variations $\delta\phi$ represent strongly coupled classical fields which precludes a perturbative strategy. Starting with a review of linear models in Sec. 2.1, we elaborate on a non-perturbative yet algebraic and thus efficient approach to the phase retrieval problem [20, 21], based on identifying an exact phase-scaling symmetry in the limit $\delta\phi \to 0$. Increasing $\delta\phi$, forward propagation continuously strengthens the explicit breaking of this phase-scaling symmetry. However, for multi-scale phase objects of a broad spectrum of spatial frequencies it turns out that this effect dominates linear contrast only within thin concentric rings in transverse Fourier space. The non-linearly (and non-locally) induced contrast, however, turns out to be marginal when compared to linearly induced contrast along the spectrum. As a consequence, these above-mentioned rings can safely be ignored when retrieving ϕ from g_z. On the other hand, *dynamical* symmetry breakdown, that is, a dependence of the radial positions of ring centers on the strength of phase upscaling, is critically delayed. These two facts reveal a definite, quasi-linear relation between $\mathscr{F}g_z$ and $\mathscr{F}\phi$ which includes a regime of sizable phase variations ($\delta\phi \sim 1$, $\mathscr{F}$ referring to transverse Fourier transformation, see Sec. 2.2). This is reminiscent of quasi particles, describing the effects of moderate interactions in terms of a (locally) renormalized free-particle dispersion relation – a ubiquitous concept in condensed-matter, particle, and plasma physics [22, 23]. Here a spatial frequency ξ serves as a "particle" label in a dispersion relation connecting (complex) "energy" $\mathscr{F}g_z(\xi)$ and (complex) "momentum" $\mathscr{F}\phi(\xi)$ in a linear way except for the above mentioned rings. Within such a ring many-to-one maps induce "energy" $\mathscr{F}g_z$ of "particle" ξ from "momenta" $\mathscr{F}\phi(\xi')$, belonging to an extended range of "particles" $\{\xi'\}$, centered at ξ. Therefore, collective effects control the emergence of non-linear contrast: the spectral contrast in the center of a ring can be considered a many-particle state. As is shown in Sec. 2.2 and Sec. 3 based on simulations, the dependences of linear contrast transfer on z and on shot noise (Sec. 2.1) as well as phase-attenuation duality all remain valid if ξ is not part of a ring. Quasi-particle phase retrieval – an inversion of the quasi-linear ϕ-g_z relation in transverse Fourier space – therefore enjoys a rather universal applicability. It should be noted though that our results do depend on the fact that a large ensemble of spatial scales is assumed to be present in the object. Intensity contrast

#251990 Received 16 Oct 2015; revised 25 Jan 2016; accepted 28 Jan 2016; published 19 Feb 2016

induced by single-scale objects starts to behave non-linearly throughout the entire spectrum for small phase modulations already [24]. In particular at small frequencies, the spectrum of the intensity contrast induced by the propagation of a single-scale phase object exhibits additional zero crossings in the far-field regime not predicted by any linear model.

In Sec. 4 we demonstrate the utility of this approach in tomographically imaging *Xenopus laevis* development both *ex* and *in vivo*. While the requirements on dose are less severe in the former case, where a practically noise-free situation can be tested by long exposures, we clearly show that comparable results in view of contrast and resolution are obtained *in vivo* at a significantly reduced dose (factor 2.5) when the propagation distance is increased from $z = 0.7\,\mathrm{m}$ to $z = 3.6\,\mathrm{m}$. In Sec. 5 we briefly summarize our results and discuss how a new generation of diffraction limited X-ray sources will boost the dose efficiency of X-ray propagation based phase-contrast tomography employing quasi-particle phase retrieval from intensity measured at a single distance in the tens of meters.

2. Pure-phase specimen

2.1. Linear Models

We first consider ideal spatio-temporal coherence in a parallel beam. Noisy contaminations in I_z then arise from indeterministic photon emissions by the radiation source, light-matter interactions within the object, quantum fluctuations of the radiation field, and the detection process itself. Effectively, we model all these influences by one and the same Poisson statistics on I_z (shot noise). In well set up *in vivo* imaging experiments, shot noise, as invoked by finite exposure times, dominates the systematic errors introduced, e.g., by monochromatization (roughness of crystal surfaces), detection (inhomogeneous scintillation, dark currents), and inhomogeneities in sample illumination. For a sufficiently small exposure time τ this causes a reduction of contrast and resolution in the retrieved 2D exit phase map as compared to the resolution limit $2\Delta x$ attained for $\tau \to \infty$. For X-rays of wavelength $\lambda = 10^{-11} \cdots 10^{-10}\,\mathrm{m} \ll \Delta x \sim 10^{-6}\,\mathrm{m}$ the diffraction is four to five orders of magnitude lower than the resolution limit set by the effective pixel size Δx.

Considering linear contrast transfer, we now provide evidence that the average NSR of g_z falls off with increasing z. Suppressing shot noise, a two-fold application of the Fresnel diffraction integral for a situation with transverse translation invariance (infinite field of view) yields [18],

$$(\mathscr{F} I_z)(\xi) = \int \mathrm{d}^2\mathbf{x}_\perp \; \psi\left(\mathbf{x}_\perp - \frac{\pi z}{k}\xi\right) \psi^*\left(\mathbf{x}_\perp + \frac{\pi z}{k}\xi\right) \times \exp\left(-2\pi \mathrm{i}\xi \cdot \mathbf{x}_\perp\right), \tag{1}$$

where ξ denotes the 2D vector of transverse spatial frequency and $k \equiv 2\pi/\lambda$. For objects lacking long-range order the exit wave field is reliably modeled as $\psi(\mathbf{x}_\perp) \equiv \sqrt{I_{\mathrm{inc}}} \exp\left[-B(\mathbf{x}_\perp) - \mathrm{i}\phi(\mathbf{x}_\perp)\right]$, B and ϕ representing beam projections of β and δ, respectively. For pure-phase objects ($B = 0$), the right-hand side of Eq. (1) expands as [21]

$$\begin{aligned}(\mathscr{F} g_z)(\xi) = {} & 2\sin(\sigma)(\mathscr{F}\phi)(\xi) \\ & - \cos(\sigma) \int \mathrm{d}^2\xi' \; (\mathscr{F}\phi)(\xi')(\mathscr{F}\phi)(\xi - \xi') \\ & + \exp(\mathrm{i}\sigma) \int \mathrm{d}^2\xi' \; \exp\left(-\mathrm{i}\frac{4\pi^2 \xi \cdot \xi' z}{k}\right) \\ & \times (\mathscr{F}\phi)(\xi')(\mathscr{F}\phi)(\xi - \xi') + \mathscr{O}\left[(\mathscr{F}\phi)^3\right], \end{aligned} \tag{2}$$

#251990 Received 16 Oct 2015; revised 25 Jan 2016; accepted 28 Jan 2016; published 19 Feb 2016

where $\sigma \equiv 2\pi^2 z\xi^2/k$. A truncation at linear order in $(\mathscr{F}\phi)$ is a valid approximation to image formation if

$$\left|\phi\left(\mathbf{x}_\perp - \frac{\pi z}{k}\xi\right) - \phi\left(\mathbf{x}_\perp + \frac{\pi z}{k}\xi\right)\right| \ll 1 \tag{3}$$

for all $\mathbf{x}_\perp$ within the field of view (FoV) and for ξ satisfying $|\xi| < \xi_c$. Here the radial spatial-frequency cutoff ξ_c is given as $\xi_c \equiv 1/(2\Delta x)$.

Conveniently, $|\delta\phi|_{\max}$ is defined as the maximum of the left-hand side of (3) over all admissible $\mathbf{x}_\perp$ and ξ. In the limit $z \to 0$, the series in Eq. (2) is dominated by the linear-in-z part of the term which is linear in $(\mathscr{F}\phi)$, corresponding to so-called Paganin phase retrieval [25]. The algebraic inversion of $(\mathscr{F}g_z)(\xi) = -\sigma(\mathscr{F}\phi)(\xi)$ imposes a low-pass filter on $(\mathscr{F}g_z)$ which introduces a second-order pole at $|\xi| = 0$. This pole is usually regularized by letting $\sigma \to \sigma + \varepsilon$ ($\varepsilon \ll 1$ a positive, real constant), see Sec. 3 for a physical interpretation. More specifically, by suppressing high-frequency information within range $\xi_c > |\xi| > \sqrt{k/4\pi z} \equiv \xi_P$, Paganin phase retrieval depletes attainable compared to maximal resolution set by $\xi_c^{-1} = 2\Delta x$, unless $\xi_c \sim \xi_P$ or $z = k(\Delta x)^2/\pi$ (edge-enhancement regime, see Fig. 2(a)). For $\mathrm{E} = 20\,\mathrm{keV}$ and $\Delta x = 1\,\mu\mathrm{m}$, this happens at $z \sim 3.2\,\mathrm{cm}$.

In vivo imaging, e.g., the development in *Xenopus laevis* (African clawed frog) [1, 2], g_z is unacceptable at such low values of z in view of the high noise-to-contrast ratio R_{g_z}, see Eq. (6) and Fig. 2(c). For contrast transfer according to the linear order in Eq. (2) this is explained by the small slope of the sine function in ξ^2 for $\sigma \ll \pi$. To discuss this further, we define the noise $\mathscr{N}Q$ of quantity Q, which depends on I_z, as the difference between Q, evaluated for a given shot-noise level of I_z, and Q, evaluated on the noise-free intensity I_z. Also, we define the dimensionless angular average of the modulus of the transverse Fourier transform of Q as

$$\widetilde{Q}(|\xi|) \equiv \frac{1}{2\pi\int_{\mathrm{FoV}} \mathrm{d}^2\mathbf{x}_\perp} \int_0^{2\pi} \mathrm{d}\varphi\, |\mathscr{F}Q|(\xi)\,. \tag{4}$$

In numerical simulations, the integral in Eq. (4) is approximated by a sum over 4 equidistant angles, $\varphi_j = \gamma + 90^\circ \cdot j$ ($j = 0, \cdots, 3$) where the offset angle $\gamma > 0$ is chosen such as to exclude on-axis truncation rods. We have checked that such a way of approximating the right-hand side of Eq. (4) does not affect any of this work's conclusion, see also [26] for a refined numerical implementation of this angular average. Moreover, the modulus of Q, averaged over the FoV (transverse average), is abbreviated as

$$\overline{Q} \equiv \frac{\int_{\mathrm{FoV}} \mathrm{d}^2\mathbf{x}_\perp\ |Q|}{\int_{\mathrm{FoV}} \mathrm{d}^2\mathbf{x}_\perp}\,. \tag{5}$$

Fig. 2(c) depicts $\log_{10} R_{g_z}$, where R_{g_z} is defined as

$$R_{g_z} \equiv \frac{\overline{\mathscr{N}g_z}}{\overline{g_z}}\,, \tag{6}$$

when prescribing a 1.5 % shot-noise level for I_z. Note that R_{g_z} is larger than unity for $z < z_1$ and falls off as $\sim z^{-1/2}$ beyond $z = z_1$ as suggested by Figs. 2(a) ($\overline{g_z} \sim z^{1/2}$ for large z) and 2(b) $\left(\widetilde{\mathscr{N}g_z}(|\xi| = 0) \le \overline{\mathscr{N}g_z}\right)$. For $|\delta\phi|_{\max} = 1$, simulated z dependences of $\overline{g}_z$ and the radial spectral moments M_1, M_2, defined as

$$M_i \equiv \frac{\int \mathrm{d}^2\xi\ (|\xi|/\xi_c)^i\, |\mathscr{F}I_z/I_0|(\xi)}{\int \mathrm{d}^2\xi\ |\mathscr{F}I_z/I_0|(\xi)}\,, \qquad (i = 1, 2)\,, \tag{7}$$

are shown in Fig. 2(a). The linear rise of function $\overline{g}_z$ at low z is dominated by local contrast growth at edges up to the peak position of M_1 and M_2 where maximum edge enhancement

#251990 Received 16 Oct 2015; revised 25 Jan 2016; accepted 28 Jan 2016; published 19 Feb 2016

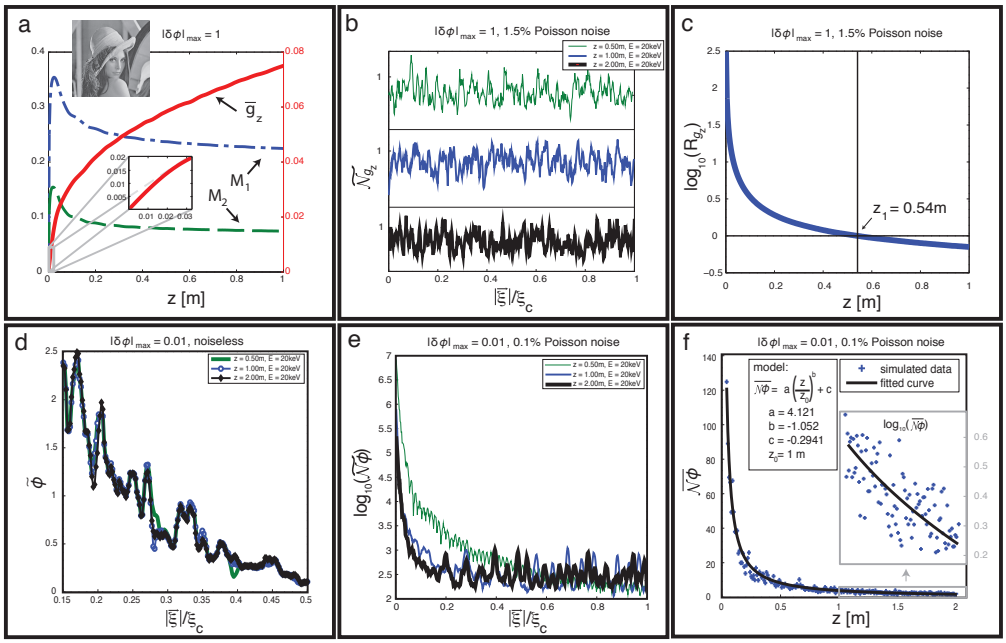

Fig. 2. Image formation in full Fresnel theory and linear phase retrieval for the pure-phase case subject to statistical noise in dependence of propagation distance z at $\mathrm{E} = 20\,\mathrm{keV}$ and $\Delta x = 1\,\mu\mathrm{m}$ using Lena as an exit phase map which is representative of broad class of pure-phase samples with a sufficiently broad frequency spectrum. A maximum exit phase variation of 1 constitutes the input for the simulated forward propagation used in (a) through (c) and of 0.01 (linear case) in (d) through (f). (a) $\overline{g}_z$ and first, second radial moments, M_1, M_2 (for definition see Eq. (7)), in dependence of z. The peak position of M_1 and M_2 indicates maximum edge enhancement. Here the right-hand side ordinate depicts the values of $\overline{g}_z$ while the left-hand side ordinate associates with the values of M_1 and M_2. (b) radial spectra $\widetilde{\mathcal{N}g_z}$ (for definition see Eq. (4)) for three distinct values of z and a Poisson noise level of 1.5 % on I_z. Note that there is no relevant z dependence of these spectra. (c) logarithm of R_{g_z} (for definition of R_{g_z}, see Eq. (6)), (d) radial spectra of retrieved phase, $\widetilde{\phi}$, from noiseless g_z for three distinct values of z. There is no dependence on z. (e) logarithm of the radial spectra of noise in retrieved phase, $\widetilde{\mathcal{N}\phi}$, induced by 0.1 % Poisson noise on I_z, for three distinct values of z. (f) transverse average of modulus of retrieved phase's noise (0.1 % Poisson noise on I_z), $\overline{\mathcal{N}\phi}$, as a function of z, see Eq. (5).

#251990 Received 16 Oct 2015; revised 25 Jan 2016; accepted 28 Jan 2016; published 19 Feb 2016

occurs. Larger values of z separate and widen the fringes, formerly "condensed at the edges, such that the image is characterized by multiple, resolvable fringe orders per edge. While the amplitude of a given fringe order saturates to certain values as z rises quantity $\overline{g}_z \propto z^{1/2}$ yet increases because of this growth of fringe multiplicity.

Keeping only the local (linear) term of Eq. (2), Figs. 2(d) and 2(e) depict $\widetilde{\phi}$ (retrieved phase based on noiseless I_z) and $\widetilde{\mathscr{N}\phi}$ (noise level of 0.1 %) for $z = 0.5\,\mathrm{m}$, $z = 1.0\,\mathrm{m}$, and $z = 2.0\,\mathrm{m}$. While $\widetilde{\phi}$ is approximately constant, both $\widetilde{\mathscr{N}\phi}$ and $\overline{\mathscr{N}\phi}$ fall off with increasing z (Fig. 2(f)). Since $\overline{\mathscr{N}\phi}$ essentially is given by $\lim_{|\xi|\to 0}\widetilde{\mathscr{N}\phi}$ and because $\mathscr{N}g_z$ is constant in z (for constancy of $\widetilde{\mathscr{N}g_z}$ in z, see Fig. 2(b)) we have $\overline{\mathscr{N}\phi} \sim z^{-1}$ as confirmed by the fit of Fig. 2(f).

Experimentally, z can not be raised indefinitely due to partial spatial coherence: Only if the blur b of I_z, introduced by the spatial extent of an incoherently emitting source (van-Cittert-Zernike theorem [27,28], propagation induced transverse coherence length $l_t = \lambda/2 \times d/s$ with d the source-object distance and s the maximal transverse extent of the source), satisfies $b = z\lambda/(2l_t) \leq 2\Delta x$ does contrast transfer from phase to intensity exhaust the 2D transverse Fourier space up to ξ_c, in compliance with Eq. (1). That is, partial transverse coherence limits z to $z \leq 4\Delta x l_t/\lambda$. For $E = 30\,\mathrm{keV}$ ($E = 20\,\mathrm{keV}$), $d = 150\,\mathrm{m}$, $s = 150\,\mu\mathrm{m}$, and $\Delta x = 1.6\,\mu\mathrm{m}$ this yields $l_t = 20.7\,\mu\mathrm{m}$ ($l_t = 30.99\,\mu\mathrm{m}$) and $z \leq 3.2\,\mathrm{m}$. On the other hand, there is a lower bound on z due to partial temporal coherence (or monochromaticity, $m \equiv \Delta E/E > 0$): the path difference for interference of X-rays emanating from two points in the exit plane, transversely separated by $|\Delta x_\perp|$, needs to be smaller than the longitudinal coherence length $l_l = \lambda E/\Delta E$ [27, 28]), given that $|\Delta x_\perp| = 2l_t$. Therefore, $z \geq 2l_t^2/l_l$. For the above numerical examples and with $m = 10^{-2}$ this yields the following allowed range(s) for z: $3.2\,\mathrm{m} \geq z \geq 0.14\,\mathrm{m}\,(0.31\,\mathrm{m})$.

2.2. *Quasi-particle transfer of contrast*

The condition $|\delta\phi|_{\max} \ll 1$ does not usually comply with the realities of *in vivo* phase-contrast tomography. For example, a 1 % relative phase shift translates into $|\delta\phi|_{\max} \sim 1.5$ when acquired by a 30 keV X-ray projection through an early-stage frog embryo of 1 mm diameter with a mean value of δ of 10^{-6}. This calls for an approximate inversion of Eq. (2) which is reliable beyond linear order. Note that to invert Eq. (2) analytically, is hopeless due to infinitely many non-local higher-order terms. On the other hand, iterative, numerical approaches are computationally inefficient and do require multiple-distance data (see, however, [29] where 3D iterative reconstruction of optical indices is facilitated by *tomographic* single-distance data). But the latter implies slow assessment of reconstructed data and a dose dilemma for X-ray *in vivo* imaging due to repeated exposures.

In constructing an adequate algebraic (local) approximation to the solution of Eq. (2) symmetry is an important guiding principle. To this end, one observes that Eq. (1) and every order in ϕ in Eq. (2) are invariant under global phase shifts

$$\psi \to \exp(-\mathrm{i}\alpha)\,\psi = \sqrt{I_{\mathrm{inc}}}\exp\left[-\mathrm{i}\left(1+\frac{\alpha}{\phi}\right)\phi\right], \quad (\alpha \ \text{ real}).$$

But the limit $|\delta\phi|_{\max} \to 0$ renders the factor $1+\alpha/\phi$ in front of ϕ a real constant S, turning an invariance under phase shifts into a symmetry under global phase *scaling*, $\phi \to S\phi$. To investigate non-linear effects in forward propagation one may ask [21] in what sense such a scaling symmetry persists at finite values of $|\delta\phi|_{\max}$.

First, upon forward propagation as simulated by the full theory, the *zeros* of $\widetilde{g}_z$ at $|\xi|_m = \sqrt{\frac{mk}{2\pi z}}$, $m = 1, 2\ldots$ (Fig. 3(b)), as predicted by the linear order in Eq. (2), transform into *minima* under phase upscaling ($S > 1$). Remarkably, when increasing the scale factor S from $S = 1$ up to critical values $S_{c_m} \gg 1$, corresponding to $|\delta\phi|_{\max}$ substantially exceeding unity, the positions

#251990 Received 16 Oct 2015; revised 25 Jan 2016; accepted 28 Jan 2016; published 19 Feb 2016

of the minima practically do not move (Fig. 3(c)), for a discussion of how this behavior is extracted from $\widetilde{g}_z$, see [26]. Such constancy requires the contribution of all orders on the right-hand side of Eq. (2): any truncation beyond linear order would have resulted into a running of the minima with increasing S. For $S > S_{c_m}$ minima of $\widetilde{g}_z$ critically start to move like order parameters through second-order phase transitions (Fig. 3(c), $m = 1,2,3$), and the existence of a finite asymptote for $m \to \infty$ is suggested: $S_{c_m} > 200, \forall m \geq 1$.

Second, denoting by $|\xi|_{m,m-1}$ the position of a maximum of $\widetilde{g}_z$ in between minima $|\xi|_m$ and $|\xi|_{m-1}$, growth ratios, defined as

$$\widetilde{g}_z\left(|\xi|_{m,m-1}\right)(S)\,/\widetilde{g}_z\left(|\xi|_1\right)(S=1)\,,$$

evolve linearly in S and strongly dominate growth ratios

$$\widetilde{g}_z\left(|\xi|_m\right)(S)\,/\widetilde{g}_z\left(|\xi|_1\right)(S=1)$$

which evolve non-linearly in S for $S \leq 200$, see Fig. 3(d) for $m = 1,2,3$. Interestingly, the latter are degenerate, indicating that, independently of S, non-linear terms in Eq. (2) conspire to add up to a periodic function in $\sigma = 2\pi^2 z\xi^2/k$.

The associated contrast transfer is a many-to-one map for frequencies whose moduli are close to $|\xi|_m$, see non-linear corrections in Eq. (2). On the other hand, frequencies of moduli near $|\xi|_{m,m-1}$ are mapped in an one-to-one fashion under contrast transfer. Since the latter dominate image formation, see Fig. 3(d), we conclude that the bulk information contained in $\mathscr{F}g_z$ is captured by linear transfer as in Fig. 3(b) while marginal non-linear effects are localized near the minima $|\xi|_m$.

Exploiting these two observations, we may consider a locally renormalized intensity contrast $\widehat{\mathscr{F}g_z}$, which neglects non-linearly induced intensity contrast, to be subjected to the linear order in Eq. (2) for phase retrieval. In contrast to the linear model, this renders the phase to be free of singularities due to first-order poles $|\xi|_m$ ($m \geq 1$). The second-order pole at $|\xi| = 0$ is regularized as in Paganin phase retrieval, see Sec. 3.

One may define $\widehat{\mathscr{F}g_z}$ as

$$\begin{aligned}(\mathscr{F}g_z)(\xi) &\to \left(\widehat{\mathscr{F}g_z}\right)(\xi)\\ &\equiv \Theta\left(|\sin(\sigma)| - \hat{\delta}\right)(\mathscr{F}g_z)(\xi)\,,\end{aligned} \tag{8}$$

where Θ denotes the Heaviside step function, and $\hat{\delta} \ll 1$ is a positive, real constant, Sec. 3 for an assessment of such a "regularization. For $\hat{\delta} \ll 1$ this constrains the support of $\left(\widehat{\mathscr{F}g_z}\right)(\xi)$ to be outside the rings $||\xi| - |\xi|_m| \leq \frac{\hat{\delta}k}{4\pi^2 z}|\xi|_m^{-1}$. Demanding continuity of $\widehat{\mathscr{F}g_z}$, one may alternatively prescribe

$$\left(\widehat{\mathscr{F}g_z}\right)(\xi) \equiv \frac{1}{\hat{\delta}}\sin(\sigma)(\mathscr{F}g_z)(\xi) \tag{9}$$

on these rings and set $\left(\widehat{\mathscr{F}g_z}\right)(\xi) = (\mathscr{F}g_z)(\xi)$ otherwise (Fig. 3(e)). In practice (e.g., soft biological tissue), no advantage of Eq. (8) over Eq. (9) is observed for phase retrieval employing $10^{-3} \leq \hat{\delta} \leq 10^{-2}$. Again, this indicates the marginality of information around the minima. Moreover, the ratio of summed ring areas A_R within disk $|\xi| \leq \xi_c$,

$$A_R = \sum_{m=1}^{2\pi z\xi_c^2/k} 2\pi|\xi|_m \frac{2\hat{\delta}k}{4\pi^2 z}|\xi|_m^{-1} = 2\hat{\delta}\xi_c^2\,,$$

#251990 Received 16 Oct 2015; revised 25 Jan 2016; accepted 28 Jan 2016; published 19 Feb 2016

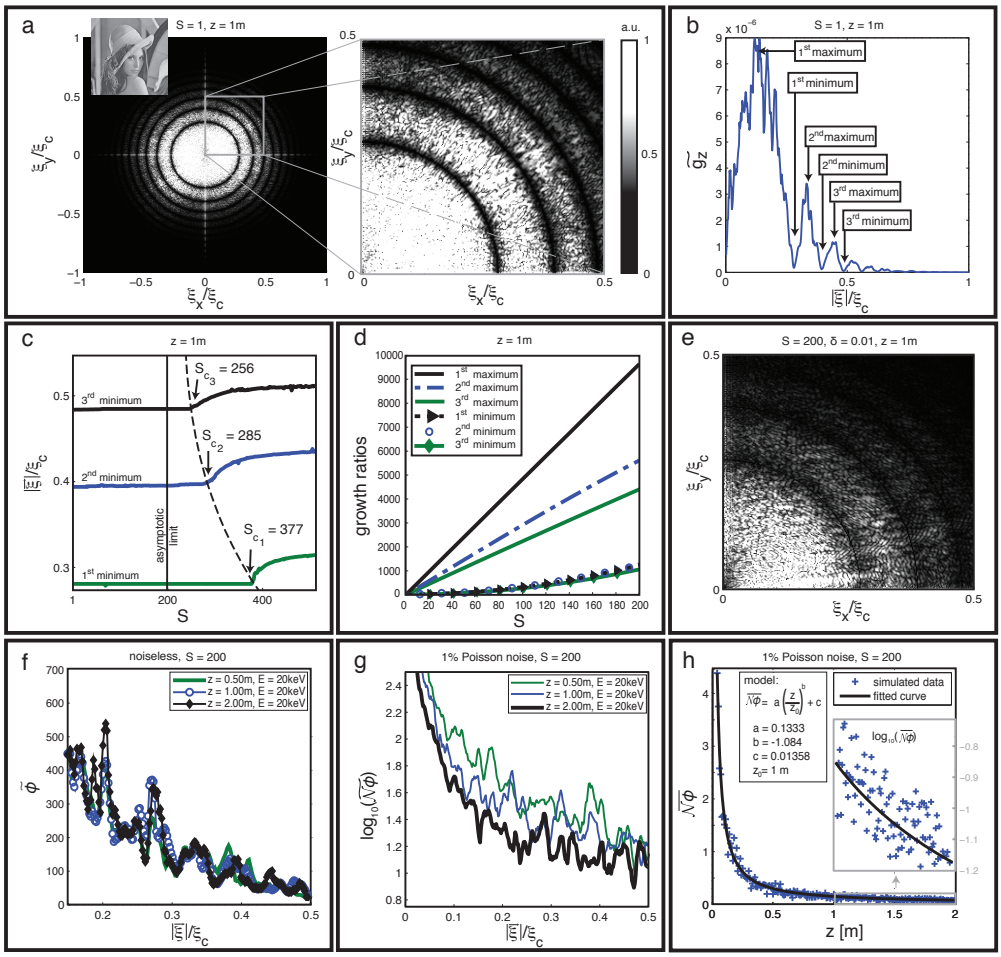

Fig. 3. Quasi-particle behavior of intensity contrast versus phase up to criticality under simulated Fresnel forward propagation at E = 20 keV. A maximum exit phase variation of 0.01 (linear case: $S = 1$), 2 (non-linear case: $S = 200$) is the input for (a) and (b), (e) through (h), respectively. In (a) through (e) $z = 1$ m was used. (a) modulus of Fourier transform of intensity contrast. (b) radial spectrum $\widetilde{g}_z$ of g_z. First three minima $|\xi|_1$, $|\xi|_2$, and $|\xi|_3$ are clearly discernible. (c) positions of $|\xi|_1$, $|\xi|_2$, and $|\xi|_3$ in dependence of S, upscaling the linear case. For the hypothetical (infinite-resolution) limit $m \to \infty$, S_{c_m} appears to converge to a finite value ~ 200. (d) S dependences of first three maxima and minima normalized to first minimum at $S = 1$ (growth ratios). Note degeneracy of curves for growth of minima. (e) modulus of Fourier transformed modified intensity contrast, defined by Eq. (9), for $\delta = 0.01$. (f) radial spectra of phase retrieved from noiseless g_z. Note an approximate z independence. (g), logarithm of the radial spectra of noise in retrieved phase, subject to 1 % Poisson noise on I_z, for three distinct values of z. (h), transverse average of modulus of retrieved phase's noise (1 % Poisson noise on I_z) as a function of z.

#251990 Received 16 Oct 2015; revised 25 Jan 2016; accepted 28 Jan 2016; published 19 Feb 2016

to this disk's area A_D ($A_D = \pi\xi_c^2$), is

$$\frac{A_R}{A_D} = 2\hat{\delta}/\pi\,.$$

This proves z-independence and smallness of the support neglected in $\left(\widehat{\mathscr{F} g_z}\right)(\xi)$ of Eq. (8).

The thus established approximate intactness of the linear relation between ϕ and g_z in Fourier space is reminiscent of quasi-particle dispersion relations. Here $(\mathscr{F}\phi)(\xi)$ can be interpreted as a (complex) "momentum" and $(\mathscr{F} g_z)(\xi)$ as a (complex) "energy" while ξ continuously labels both "particle" species away from $|\xi|_m$ and degenerate "ground states" near $|\xi|_m$. Hence, for $S < S_{c_m}$ ($m = 1,2,3,\cdots$), scaling symmetry, albeit explicitly broken by the non-linear orders in Eq. (2) and associated with a finite value of the "ground-state energy", remains dynamically unbroken: the "ground states" $|\xi|_m$ themselves are nearly invariant under phase upscaling.

For $S = 200$, $\hat{\delta} = 10^{-2}$, noiseless g_z, and three distinct values of z Fig. 3(f) shows radial phase spectra $\widetilde{\phi}$ as retrieved in the quasi-particle approach. As in the linear case (Fig. 2(d)), $\widetilde{\phi}$ is nearly independent of z. This, again, indicates that all non-linear terms in Eq. (2) add up to a small correction to the linear behavior. At a shot-noise level of 1 %, the behavior of $\widetilde{\mathscr{N}\phi}$ (Fig. 3(g)) is essentially identical to the linear case (Fig. 2(e)). This is also true of $\overline{\mathscr{N}\phi}$ (Fig. 3(h), same z^{-1} decay as in Fig. 2(f)).

3. Global phase-attenuation duality

In single-distance phase retrieval, absorptive effects can be taken into account by assuming global phase-attenuation duality (GPAD) [31–33] (see [34, 35] for a more local approach). GPAD posits that $B(\mathbf{x}_\perp) = \varepsilon\phi(\mathbf{x}_\perp)$, where ε is a small, real, and positive constant. This breaks the global phase-shift symmetry of Fresnel theory. GPAD is approximately valid for hard X-rays when quasi-free valence electrons dominate light-matter interaction (Compton scattering) [34], and/or for chemically homogeneous samples [35]. Under GPAD the linear term in Eq. (2) generalizes as

$$\begin{aligned}(\mathscr{F} g_z)(\xi) &= -2\left(\sin(\sigma) + \varepsilon\cos(\sigma)\right)(\mathscr{F}\phi)(\xi)\\ &= -2\sqrt{1+\varepsilon^2}\sin(\sigma + \arctan\varepsilon)(\mathscr{F}\phi)(\xi)\,.\end{aligned} \tag{10}$$

In Eq. (10) the sine function's simple zeros thus are shifted to the left,

$$|\xi|_m \to \sqrt{\frac{mk}{2\pi z}}\left(1 - \frac{\varepsilon}{2\pi m}\right) + \mathscr{O}(\varepsilon^2)\,,\quad (m \geq 1, \varepsilon \leq 1)\,. \tag{11}$$

At an X-ray energy of $\sim 20\,\mathrm{keV}$ and imaging soft biological tissue, one has $\varepsilon \sim 0.5\times 10^{-3}$. Hence a relative shift of $\mathscr{O}\left(10^{-4}\right)$ is implied for $|\xi|_m$ at $m = 1,2,3$. Notice that the double zero $|\xi|_0 = 0$ of $\mathscr{F} g_z$ splits into $|\xi|_0 = \pm\mathrm{i}\sqrt{\varepsilon k/(2\pi^2 z)}$ at finite B. Thus the presence of the associated singularity at $|\xi|_0 = 0$ in the retrieved phase is prevented by absorptive effects. Fig. 4(a) shows S and ε dependences of the minima $|\xi|_m$ in the forward simulated function $\widetilde{g}_z$ for $10^{-2} \geq \varepsilon \geq 10^{-3}$, demonstrating that the critical behavior is retained in the movement of the minima $|\xi|_m$ under phase upscaling for realistic values of ε. We mention in passing that the growth ratios at $\varepsilon > 0$ are essentially those of Fig. 3(d).

4. *Ex* and *in vivo* X-ray phase-contrast microtomography and *Xenopus laevis* development

We now report on applications of X-ray phase contrast microtomography (XPCμT). Fig. 4(b) depicts g_z (left) and $|\mathscr{F} g_z|$ (right), obtained from a propagated, *ex vivo* projected *Xenopus laevis* embryo at 4-cell stage.

#251990 Received 16 Oct 2015; revised 25 Jan 2016; accepted 28 Jan 2016; published 19 Feb 2016

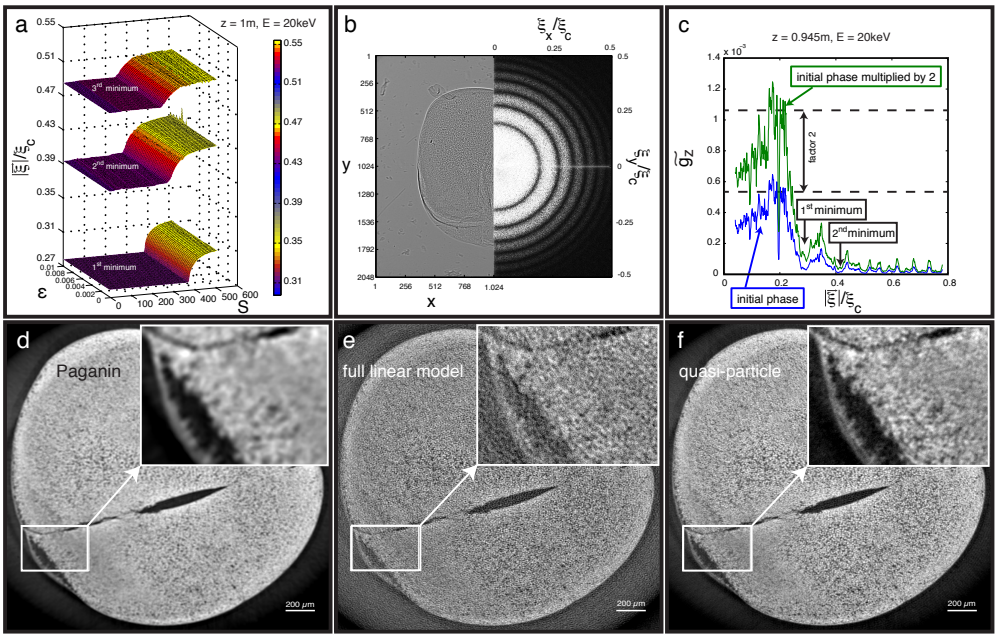

Fig. 4. Global phase-attenuation duality vs. upscaling and confrontation with experimental data on fixed frog embryo. (b) through (f) are based on tomographic data, representing a fixed, 4-cell stage *Xenopus laevis* embryo, see Appendices A,C and Visualization 1. (a) dependence of 1st, 2nd, and 3rd minimum of $\widetilde{g_z}$ as a function of S and the duality parameter ε for $0 \leq \varepsilon \leq 10^{-2}$ in simulated forward propagation using Lena as a phase pattern ($\delta\phi_{\max} = 0.01$ at $S = 1$). Note stability of the critical behavior in S under variations of ε. (b) g_z for a fixed projection angle (left) and modulus of Fourier transform, $|\mathscr{F} g_z|$, (right). The visibility of several rings demonstrates the presence of information at high frequencies which would be suppressed by Paganin phase retrieval. (c) g_z in blue is obtained from experiment; g_z in green results from forward-propagation after upscaling by a factor of two of the quasi-particle retrieved phase $\delta\phi$ ($\varepsilon = 10^{-2.5}$, $\delta = 0.1$, see Appendix B), (d), (e), and (f) equal slice through tomographic reconstruction after Paganin phase retrieval, phase retrieval using Eq. (10), and its quasi-particle version, respectively.

This data was acquired with beamline ID 19 of European Synchrotron Radiation Facility (Appendix). With a quasi-monochromatic flux density of 10^{12} photons/(mm^{2}s), 2 s of exposure per projection, and a conversion efficiency for X-rays to visible light of about 5 % the number of events per pixel and exposure is about 5.4×10^4. Thus a low shot-noise level of 0.42 % occurs (clearly discernible rings with radii up to $\xi_c/2$ in Fig. 4(b), right panel). Self-consistency of the quasi-particle approach is evidenced by the constancy of $|\xi|_m$ in $\frac{1}{2\pi}\int_0^{2\pi} \mathrm{d}\varphi \left|\mathscr{F} g_z^{\mathrm{fluct}}\right|$ under upscaling of the retrieved phase $\delta\phi$ as $\delta\phi \to 2\delta\phi$ and subsequent simulated forward propagation (Fig. 4(c), Appendix B for definitions of g_z^{fluct} and $\delta\phi$). A slice of reconstructed volume is shown for Paganin phase retrieval (Fig. 4(d)), using the full linear model (Fig. 4(e)), and quasi-particle phase retrieval (Fig. 4(f), Visualization 1 of Appendix C). This clearly demonstrates the improved resolution of the shape and distribution of yolk platelets and the cell membrane (single membrane in Fig. 4(d), double membrane in Fig. 4(f); Visualization 4 of Appendix C). Note the poor quality of the full linear model which is due to the poles in the retrieved phase at $|\xi|_m$ in Fourier space (Fig. 4(e)).

In vivo XPCμT data were acquired with beamline 32-ID at Advanced Photon Source

#251990 Received 16 Oct 2015; revised 25 Jan 2016; accepted 28 Jan 2016; published 19 Feb 2016

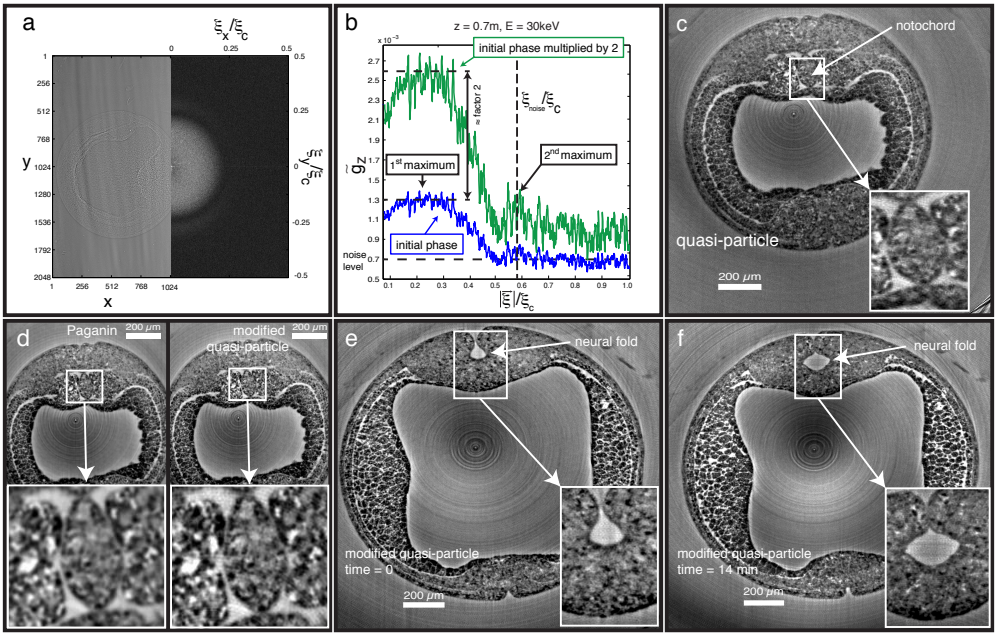

Fig. 5. *In vivo* XPCμT of *Xenopus laevis* development within stage-19 embryo (late neural stage) as imaged at beamline 32-ID of APS. (a) intensity contrast g_z of posterior part at fixed projection angle (left), and modulus of Fourier transform, $|\mathscr{F} g_z|$, (right). Ring orders higher than second are washed out by shot noise. (b) $\widetilde{g}_z$ in blue is obtained from experiment; $\widetilde{g}_z$ in green results from simulated forward propagation after upscaling by a factor of two of the quasi-particle retrieved phase $\delta\phi$ ($\varepsilon = 0$, $\delta = 0.1$). The vertical dashed line indicates the frequency cutoff ξ_{noise}, chosen such as to discriminate signal-dominating noise, see text. (c) reconstructed dorsal-ventral slice using quasi-particle phase retrieval. (d) reconstruction of same slice using Paganin (left) and modified quasi-particle (right) phase retrieval (Eq. 12). The former sacrifices resolution by neglecting frequencies higher than the first maximum of $\widetilde{g}_z$, the latter cuts off shot-noise dominated frequencies beyond the second maximum (b). (e) reconstruction of more posterior dorsal-ventral slice subject to modified quasi-particle phase retrieval. (f) same reconstruction of same slice as in (e) but now after 14 min time lapse. Comparing (e) and (f), note closing of neural tube.

(APS, $z = 0.7\,\mathrm{m}$) and with beamline ID19 at European Synchrotron Radiation Facility (ESRF, $z = 3.6\,\mathrm{m}$) (for details on experimental parameters see Appendix A). Development of stage-19 *Xenopus laevis* embryos (neural groove stage) was imaged in terms of volumes, temporally separated by a 14 min (APS) and a 12 min (ESRF) time-lapse.

Fig. 5(a) shows g_z (left) and $|\mathscr{F} g_z|$ (right) for one and the same projection at time 0. An approximate (monochromatic) flux density of 10^{12} photons/(mm^{2}s) X-ray photons, 60 ms of exposure per projection, and a conversion efficiency for X-rays to visible light of about 10 % here implies an event number of about 10^4 per pixel and exposure and an associated shot-noise level of 1 %. This noise level is considerably higher than for the above *ex vivo* situation and causes invisibility of higher-order rings where noise dominates signal (Fig. 5(a) (right)). As in Fig. 4(c) self-consistency of the quasi-particle approach is tested by upscaling the retrieved phase and a subsequent, simulated forward propagation (Fig. 5(b)). Here $g_z \equiv I_z/\bar{I}_z - 1$ (Appendix B). The vertical dashed line indicates the frequency cutoff $\xi_{\mathrm{noise}} = |\boldsymbol{\xi}|_{2,1}$, chosen such as to remove noise dominated, high frequencies. Accordingly, the renormalized intensity con-

#251990 Received 16 Oct 2015; revised 25 Jan 2016; accepted 28 Jan 2016; published 19 Feb 2016

trast $\left(\widehat{\mathscr{F}g_z}(\xi)\right)$ of Eq. (8) or Eq. (9) modifies as

$$\left(\widehat{\mathscr{F}g_z}(\xi)\right) \to \Theta\left(\xi_{\text{noise}} - |\xi|\right)\left(\widehat{\mathscr{F}g_z}(\xi)\right). \tag{12}$$

Interestingly, reconstruction results do not depend on whether $\Theta\left(\xi_{\text{noise}} - |\xi|\right)$ is replaced by a filter with a softer transition. Fig. 5(c) shows a reconstructed slice at time 0 using quasi-particle phase retrieval according to Eq. (8). Compared to quasi-particle phase retrieval subject to the modified intensity contrast of Eq. (12), this impairs contrast, see Fig. 5(d) (right) (APS) and Visualization 5 of Appendix C (ESRF). On the other hand, Paganin phase retrieval (Fig. 5(d) (left)), which discriminates high-frequency noise but also cuts off information from maximum $|\xi|_{1,0}$ onwards, exhibits poorer resolution (Visualization 6 of Appendix C). The same reconstructed slice at time 0 and time 14 min is depicted in Figs. 5(e) and 5(f) (Visualizations 2,3 of Appendix C for 3D representations). In comparing Figs. 5(e) with 5(f), note the closing of the neural tube, indicating development. To demonstrate the increased dose efficiency when employing large propagation distances we show 3D representations of one and the same, living stage-19 embryo, imaged at ESRF, in Visualizations 7,8 of Appendix C. Employing modified quasi-particle phase retrieval, the left-hand sides exhibit resolution and contrast comparable to those of Visualizations 2,3 of Appendix C. The event rates per pixel underlying the reconstructions in Visualizations 7,8 of Appendix C are, however, considerably lower ($N \sim 4.000$ compared to $N \sim 10.000$). Notice that Paganin phase retrieval, again, leads to significantly reduced 3D image resolution (right-hand sides in Visualizations 7,8 of Appendix C). A comparison of a similar, central slice in stage-19, *in vivo* data, acquired at APS ($z = 0.7\,\text{m}$, $N \sim 10.000$) and at ESRF ($z = 3.6\,\text{m}$, $N \sim 4.000$) is also presented in Fig. (6) together with a confrontation between reconstructions using Paganin and modified quasi-particle phase-retrieval. Note the improvement of resolution going from Paganin to modified quasi-particle phase-retrieval and a similar resolution using quasi-particle phase-retrieval when comparing APS and ESRF data sets.

5. Discussion

Our analysis in Sec. 2 demonstrates that phase noise, as induced by a given shot-noised intensity at a single propagation distance z, decreases like z^{-1} upon quasi-particle retrieval. Increasing z, this modality exploits the improved contrast g_z as induced by a larger weight at low frequencies. Both Paganin and quasi-particle phase retrieval exploit this effect. On the other hand, quasi-particle phase retrieval includes the information at higher frequencies (up to a noise determined cutoff) such that both contrast *and* resolution are improved when z is increased. For intensity contrast, emergent from considerable phase variations at object exit, as encountered, e.g., by hard X-ray phase-contrast micro-tomography (XPCμT) of soft organisms, this affords a powerful yet simply implementable and computationally efficient phase-retrieval algorithm.

Imaging *in vivo*, our present results employing modified quasi-particle phase retrieval indicate an improvement in resolution compared to the conventional approach (Fig. 5(d); Visualizations 5,6, Appendix C) at relatively low propagation distances of $\sim 1\,\text{m}$ imposed by the current source sizes of 3rd-generation synchrotrons. By increasing z from 0.7 m to 3.6 m using two beamlines at different synchrotrons a clearly improved dose efficiency could be demonstrated in the present work (Fig. 6; Visualizations 2,3, Appendix C versus Visualizations 7,8, Appendix C). This suggests a great potential of future diffraction limited X-ray sources for *in vivo* XPCμT imaging. Namely, exploiting the high spatial coherence of their synchrotron radiation, z values in the tens of meters can be envisaged. To enhance the associated small beam sizes (in the square-micron range) such as to still contain extended cell populations or entire embryos (linear extent l in the hundreds of microns), the sample would have to be placed a dis-

#251990 Received 16 Oct 2015; revised 25 Jan 2016; accepted 28 Jan 2016; published 19 Feb 2016

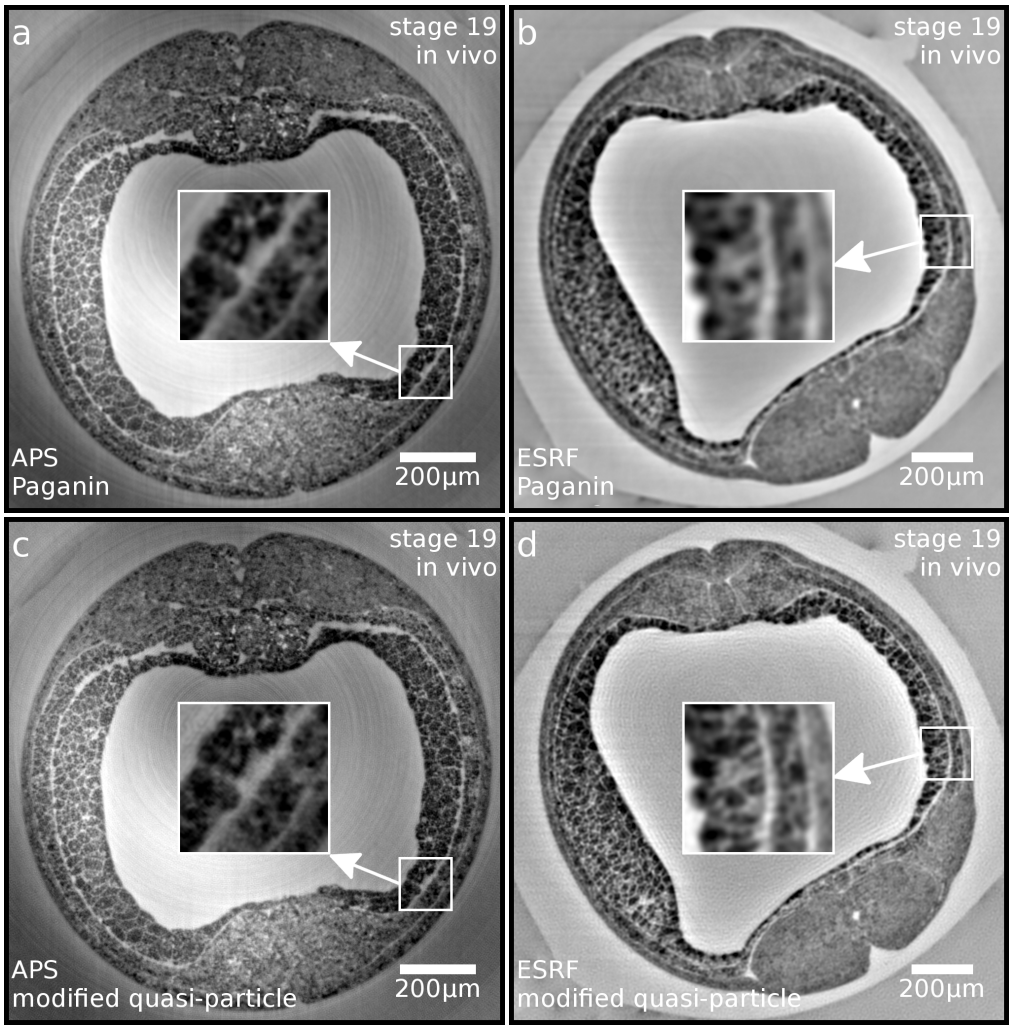

Fig. 6. *In vivo* XPCµT of *Xenopus* embryo at stage-19 (late neurula) as imaged at beamlines 32-ID of APS ((a) and (c), $z = 0.7\,\mathrm{m}$, $\Delta x = 1.3\,\mu\mathrm{m}$, and event number per pixel of $N \sim 10.000$) and ID19 of ESRF ((b) and (d), $z = 3.6\,\mathrm{m}$, $\Delta x = 1.6\,\mu\mathrm{m}$, and event number of $N \sim 4.000$). In both cases, the first member of the time-lapse series is visualized. Compared is a central slice, reconstructed with 499 projections, and acquired at similar X-ray energies $E = 30\,\mathrm{keV}$ (APS) and $E = 26.2\,\mathrm{keV}$ (ESRF). Reconstructions are based on Paganin phase retrieval ((a) and (b)) and modified quasi-particle phase retrieval ((c) and (d)).

tance R downstream of the focal spot of a focussing X-ray optics. For $l = 200\,\mu\mathrm{m}$ and $R = 4\,\mathrm{m}$ a beam divergence (bd) of 0.05 mrad would be required which is achievable with presently available Kirkpatrick-Baez mirrors [36]: $\mathrm{bd} = \lambda/\mathrm{fss}$ where fss denotes the focal-spot size. Thus, for $E = 30\,\mathrm{keV}$, which corresponds to $\lambda = 4.13 \times 10^{-11}\,\mathrm{m}$, $\mathrm{fss} \sim 1\mu\mathrm{m}$. This would generate geometric magnification $M = 1 + z/R$ and rescale z to the parallel beam situation as

$$z \to \frac{z}{M} = \left(1 - \frac{1}{M}\right) R$$

(Fresnel scaling [25]). Working with, say, $M = 20$, roughly yields $z/M = R$. To apply the same

#251990 Received 16 Oct 2015; revised 25 Jan 2016; accepted 28 Jan 2016; published 19 Feb 2016

dose as in present-day *in vivo* XPCμT, the effective pixel size Δx would have to be comparable to $\sim 1\,\mu$m. In indirect detection systems no optical-light magnification thus is required for physical pixel sizes of $\sim (20\,\mu\text{m})^2$ (high photon collection efficiency, numerical aperture equals unity). As a consequence, such a setup would populate high frequencies with intensity-contrast information. The price to pay is a $\sim 100\,$m long beam-propagation vacuum tube downstream of the sample to prevent air absorption. In addition to this vacuum pipe, the setup would consist of two small hutches, one for the sample environment, one for image detection. Under these imaging conditions, the modality of *in vivo* XPCμT proposed in the present work should generate micron resolved 3D images of a high contrast and considerably increased lengths of the associated time-lapse series.

Appendix A: Experimental conditions for ex and in vivo XPCμT

In simulating the Fresnel forward propagation of an exit wave field we applied the Fourier convolution theorem [25]. The test image Lena (512 x 512 pixels) was centrally zero padded to 1024 x 1024 pixels in transverse position space. Intensity contrast depicted in Fig. 1(b) was acquired with bending-magnet beamline TOPO-TOMO at Anströmquelle Karlsruhe (ANKA) under parallel-beam incidence, imaging *ex vivo* a *Xenopus* embryo radiographically at stage 10.5 (X-ray energy: $\text{E} = 12\,$keV; bandwidth of multilayer monochromator: $\Delta\text{E}/\text{E} = 10^{-2}$; effective pixel size: $\Delta x = 1\,\mu$m; scintillator: Lu_2SiO_5:Ce of $24\,\mu$m thickness; exposure time for the projection: 180 s; embryo embedded in agarose within Eppendorf tube of diameter 0.6 cm, see also [2]).

The stage-19 frog embryo (same sample environment) was imaged *in vivo* under parallel-beam incidence using undulator beamline 32-ID at the Advanced Photon Source (APS) (X-ray energy: 30 keV; bandwidth of Si 111 double crystal monochromator: $\Delta\text{E}/\text{E} = 10^{-4}$; propagation distance: $z = 0.7\,$m; effective pixel size: $\Delta x = 1.3\,\mu$m; FoV of 2560 x 2160 pixels; scintillator: LuAG:Ce of $100\,\mu$m thickness; exposure time per projection: $60\,\mu$s; number of tomographic projections in a 180° scan: 499) and undulator beamline ID19 at European Synchrotron Radiation Facility (ESRF) (X-ray energy: 26.2 keV; bandwidth of single-line harmonic (no monochromator : $\Delta\text{E}/\text{E} = 3 \times 10^{-2}$; propagation distance: $z = 3.6\,$m; effective pixel size: $\Delta x = 1.6\,\mu$m; FoV of 2048 x 2048 pixels; scintillator: LuAG:Ce of $100\,\mu$m thickness; exposure time per projection: $20\,\mu$s; number of tomographic projections in a 180° scan: 499). The time lapse between tomographic scans was 14 min at APS and 12 min at ESRF, commensurate with maximal endodermal cell speeds of $1\,\mu\text{m}\,\text{min}^{-1}$ and the demand that such an endodermal cell of diameter $\sim 30\,\mu$m half overlaps with itself after a single time lapse.

The estimated (van-Cittert-Zernike theorem) horizontal (vertical) transverse coherence length $l_t^{h,v} = \lambda/(2s^{h,v})d$ (d the parallel-beam source-sample distance, $s^{h,v}$ the horizontal (vertical) source size giving rise to a beam provided by a 3rd generation synchrotron facility like APS and ESRF) at the position of the sample ($d = 70\,$m, $s^h = 120\,\mu$m, $s^v = 10\,\mu$m at APS; $d = 150\,$m, $s^h = 120\,\mu$m, $s^v = 10\,\mu$m at ESRF;) is $l_t^h = 12.1\,\mu$m ($l_t^v = 145\,\mu$m) at APS and $l_t^h = 25.9\,\mu$m ($l_t^v = 310\,\mu$m) at ESRF.

Thus, $b^h = 1.2\,\mu\text{m} < 2\Delta x = 2.6\,\mu$m ($b^v = 0.1\,\mu\text{m} < 2\Delta x = 2.6\,\mu$m) at APS and $b^h = 2.9\,\mu\text{m} < 2\Delta x = 3.2\,\mu$m ($b^v = 0.24\,\mu\text{m} < 2\Delta x = 3.2\,\mu$m) at ESRF. Note that the estimates on $l_t^{h,v}$ represent lower bounds on the actual values since in addition to propagation-induced there is intrinsic coherence in undulator radiation. The longitudinal coherence length is $l_l = 0.41\,\mu$m at APS and $l_l = 0.001\,57\,\mu$m at ESRF which, by virtue of $z \geq (l_t^h)^2/(2l_l)$, implies that $z > 0.2\,$mm at APS and $z > 21.4\,$cm at ESRF.

The fixed 4-cell stage embryo (same sample environment) was imaged using undulator beamline ID19 at European Synchrotron Radiation Facility (ESRF) under parallel-beam incidence (X-ray energy: 20 keV; bandwidth of Si 111 double crystal monochromator: $\Delta\text{E}/\text{E} = 10^{-4}$;

#251990 Received 16 Oct 2015; revised 25 Jan 2016; accepted 28 Jan 2016; published 19 Feb 2016

propagation distance: $z = 0.945\,\mathrm{m}$; effective pixel size: $\Delta x = 0.75\,\mu\mathrm{m}$; FoV of 2048 x 2048 pixels; scintillator: $Gd_3Ga_5O_{12}$ of 13 µm thickness; exposure time per projection: 2 s; number of tomographic projections in a 360° scan: $N = 1599$). The estimated (van-Cittert-Zernike theorem) horizontal (vertical) transverse coherence length at the position of the sample ($d = 150\,\mathrm{m}$, $s^h = 150\,\mu\mathrm{m}$, $s^v = 10\,\mu\mathrm{m}$) is $l_t^h = 31\,\mu\mathrm{m}$ ($l_t^v = 465\,\mu\mathrm{m}$). Thus, $b^h = 0.95\,\mu\mathrm{m} < 2\Delta x = 1.5\,\mu\mathrm{m}$ ($b^v = 0.063\,\mu\mathrm{m} < 2\Delta x = 1.5\,\mu\mathrm{m}$). The longitudinal coherence length is $l_l = 0.62\,\mu\mathrm{m}$ which entails that $z > 0.8\,\mathrm{mm}$.

Image acquisition, image pre-processing, phase retrieval, and tomographic reconstruction employing Filtered Back Projection were performed as described in [2].

Appendix B: Single-distance phase retrieval and phase-attenuation duality

In practice, phase retrieval using Eq. (10) of the main text or its quasi-particle version proceeds as follows. A split $\phi = \delta\phi + \overline{\phi}$ of physical exit phase ϕ into a fluctuating part $\delta\phi$ of zero transverse mean, $0 = \frac{\int_{\mathrm{FoV}} \mathrm{d}^2\mathbf{x}_\perp\, \delta\phi}{\int_{\mathrm{FoV}} \mathrm{d}^2\mathbf{x}_\perp}$, and a constant offset $\overline{\phi}$ predicts that $g_z = \exp\left(-2\varepsilon\overline{\phi}\right) \frac{I_z^{\mathrm{fluct}}}{I_{\mathrm{inc}}} - 1$. Here I_z^{fluct} represents intensity that would emerge from $\delta\phi$ alone, and $g_z^{\mathrm{fluct}} \equiv \frac{I_z^{\mathrm{fluct}}}{I_{\mathrm{inc}}} - 1$. For $\varepsilon \ll 1$ the absorptive factor in the exit wave field can be approximated as $\exp\left(-\varepsilon\overline{\phi} - \varepsilon\delta\phi\right) \sim (1 - \varepsilon\delta\phi)\exp\left(-\varepsilon\overline{\phi}\right)$. Thus $\delta\phi$ does not reduce the mean intensity at exit, $1 = \frac{\int_{\mathrm{FoV}} \mathrm{d}^2\mathbf{x}_\perp\, (1-2\varepsilon\delta\phi)}{\int_{\mathrm{FoV}} \mathrm{d}^2\mathbf{x}_\perp}$, and the conservation of mean intensity in free-space propagation implies that $1 = \frac{\int_{\mathrm{FoV}} \mathrm{d}^2\mathbf{x}_\perp\, I_z^{\mathrm{fluct}}}{\int_{\mathrm{FoV}} \mathrm{d}^2\mathbf{x}_\perp\, I_{\mathrm{inc}}}$ or $0 = \frac{\int_{\mathrm{FoV}} \mathrm{d}^2\mathbf{x}_\perp\, g_z^{\mathrm{fluct}}}{\int_{\mathrm{FoV}} \mathrm{d}^2\mathbf{x}_\perp}$. Thus $\overline{\phi} = -\frac{1}{2\varepsilon}\log\left(\frac{\int_{\mathrm{FoV}} \mathrm{d}^2\mathbf{x}_\perp\, g_z}{\int_{\mathrm{FoV}} \mathrm{d}^2\mathbf{x}_\perp} + 1\right)$, and $\delta\phi$ can be retrieved according to the quasi-particle version of Eq. (10) of the main text upon the substitutions $g_z \to g_z^{\mathrm{fluct}}$, $\phi \to \delta\phi$. In retrieving $\overline{\phi}$ and $\delta\phi$ from the experimental data of Fig. 4(b), we have set $\delta = 10^{-1}$ and $\varepsilon = 10^{-2.5}$ (in principle, ε can be extracted from a two-distance measurement [35]). This value of ε is greater than that of water, $\varepsilon_{\mathrm{water}} \sim 0.5 \times 10^{-3}$ [3], explained by the fact that the 3D reconstruction exhibits unphysical large-scale modulations if $\varepsilon_{\mathrm{water}}$ is used for phase retrieval. We interpret this as a violation of global phase-attenuation duality, $\varepsilon = \mathrm{const} = \frac{\mathscr{F}B(\xi)}{\mathscr{F}\phi(\xi)}$, at small frequencies. From the transverse average of g_z a value $\overline{\phi} \sim 100$ was inferred, roughly matching the estimate obtained by projecting through water [3]. Fig. 4(e) is based on phase retrieval according to Eq. (12) of the main text with the sine function replaced by $\frac{1}{\mathrm{sgn}\left(\sin(\sigma + \arctan\varepsilon)\right)}\left(\left|\sin\left(\sigma + \arctan\varepsilon\right)\right| + \arctan\varepsilon\right)$. This prescription is superfluous when employing quasi-particle phase retrieval.

Appendix C: Captions on Visualizations

Visualization 1: Parallel slicing through tomographic reconstruction of entire 4-cell stage *Xenopus* embryo, imaged *ex vivo* by XPCµT using single-distance, quasi-particle phase retrieval. This 3D representation associates with Figure 4f.

Visualization 2: Parallel slicing through tomographic reconstruction of entire stage-19 *Xenopus* embryo, imaged *in vivo* by XPCµT at beamline 32-ID of APS, using single-distance, modified quasi-particle phase retrieval. A propagation distance of $z = 0.7\,\mathrm{m}$ and ~ 10.000 events per pixel were used. This 3D representation associates with Figure 5e.

Visualization 3: Parallel slicing through tomographic reconstruction of entire stage-19 *Xenopus* embryo, imaged *in vivo* by XPCµT at beamline 32-ID of APS, using single-distance, modified quasi-particle phase retrieval. A propagation distance of $z = 0.7\,\mathrm{m}$ and ~ 10.000 events per pixel were used. This 3D representations associates with Figure 5f.

Visualization 4: Comparison of reconstructed region of interest, shown in Figure 4d, 4f using

#251990 Received 16 Oct 2015; revised 25 Jan 2016; accepted 28 Jan 2016; published 19 Feb 2016

Paganin and quasi-particle phase retrieval.

Visualization 5: Comparison of quasi-particle versus modified quasi-particle based reconstruction of stage-19 *Xenopus* embryo (region of interest in a single, reconstructed slice), imaged *in vivo* by XPCμT at beamline ID19 of ESRF, at two consecutive points in time. Left-hand side shows modulus of Fourier transformed intensity contrast together with quasi-particle filters. Right-hand sides indicates associated, reconstructed slice.

Visualization 6: Comparison of reconstructed region of interest, shown in Figure 5d, using Paganin and modified quasi-particle phase retrieval.

Visualization 7: Parallel slicings through tomographic reconstructions of entire stage-19 *Xenopus* embryo, imaged *in vivo* by XPCμT at beamline ID19 of ESRF, using single-distance, modified quasi-particle (left) and Paganin (right) phase retrieval. A propagation distance of $z = 3.6\,\mathrm{m}$ and ~ 4.000 events per pixel were used.

Visualization 8: Parallel slicings through tomographic reconstructions of entire stage-19 *Xenopus* embryo, imaged *in vivo* by XPCμT at beamline ID19 of ESRF, using single-distance, modified quasi-particle (left) and Paganin (right) phase retrieval. A propagation distance of $z = 3.6\,\mathrm{m}$ and ~ 4.000 events per pixel were used. Visualization 8 represents the same living embryo as Visualization 7 subject to a time lapse of 12 min.

Acknowledgments

We acknowledge the European Synchrotron Radiation Facility (ESRF) for provision of synchrotron radiation facilities and the hospitality of Joost Batenburg's group at the Center for Mathematics and Informatics (CWI) in Amsterdam where part of this work was discussed and carried out. We are grateful for support by Francesco de Carlo's group at the Advanced Photon Source, where experimental work was performed and is foreseen which has stimulated the present analysis. This research partially was funded by COST action MP-1207 and the German Federal Ministry of Education and Research under grant numbers 05K12CK2 and 05K12VH1.

#251990 Received 16 Oct 2015; revised 25 Jan 2016; accepted 28 Jan 2016; published 19 Feb 2016